



Contents lists available at ScienceDirect

ISA Transactions

journal homepage: www.elsevier.com/locate/isatrans

Practice article

Compliant human–robot object transfer based on modular 3-axis force sensor for collaborative manufacturing

Hongliang Hua^{a,b,*}, Zhenqiang Liao^b, Yuhang Liu^c, Xiaofeng Wu^a, Jingbo Zhao^a, Jie Song^b^a School of Aeronautics and Mechanical Engineering, Changzhou Institute of Technology, Changzhou, Jiangsu 213032, PR China^b School of Mechanical Engineering, Nanjing University of Science and Technology, Nanjing, Jiangsu 210094, PR China^c School of Mechanical and Electronic Engineering, Nanjing Forestry University, Nanjing, Jiangsu 210037, PR China

ARTICLE INFO

Article history:

Received 25 January 2023

Received in revised form 4 July 2023

Accepted 4 July 2023

Available online xxxx

Keywords:

Grasping
Interaction
Force control
Force sensor
Cost-effective

ABSTRACT

The primary motivation of this paper is to present a compliant and cost-effective solution for object transfer between human and robot. The application prospect of this study is robot–human collaboration in manufacturing. To achieve above goals, a novel modular 3-axis force sensor is proposed for the grasping system to achieve interactive force sensing. Compliant object transfer control strategy, which is composed of incremental force control mode and gravity balance control mode, is proposed for object transfer between human and robot. A prototype of underactuated grasping system which is mounted on the proposed modular 3-axis force sensor is fabricated to investigate the effectiveness of the proposed interactive control strategy. Experimental results reveal that the incremental force control mode is suitable for the lighter objects with a higher interactive sensitivity. For transferring heavier objects, the gravity balance control mode is more suitable. In gravity balance control mode, the human hand could achieve a quasi-static equilibrium with the object, and achieve a compliant transfer operation. Due to the above characteristic, the proposed control strategy has the potentials to enhance the object transfer compliance and safety in the human–robot object transfer process.

© 2023 ISA. Published by Elsevier Ltd. All rights reserved.

1. Introduction

In recent years, the demand for human–robot interaction has been growing rapidly with the wide application of robotics, which has covered a variety of fields, such as precision assembly [1,2], polishing [3–6], medical rehabilitation [7–10], livelihood [11] and new generation of retail [12]. Compliant object transfer between the human and robot is a critical operation in interactive robotic applications [13]. How to precept the interactive force and achieve compliant object transfer control in a cost-effective way is a challenge problem in the robotic community [14,15].

1.1. Related work

In previous studies, machine vision [16,17] has been widely utilized to precept the interaction information for the human–robot interaction. Through vision camera, both the position, posture and shape of the object could be precepted. Therefore, the vision method has an ideal versatility for different kinds of daily supplies [18]. Since the weight of daily necessities is relatively

light, which is generally less than 0.5 Kg, the object could be transferred from the robot to the human hand in a compliant way. As the object weight increases, the vision-based object transfer could exhibit a noncompliant process. Because it is difficult for the vision camera to precept the object gravity as well as the interactive force between the human hand and object. In the heavier object transfer process, the object gravity could be applied to the human hand suddenly and affect the compliance of the human–robot interaction.

Compared to the vision camera approach, force-based interactive control strategy could achieve a more compliant effect. In recent years, the multi-axis force sensor has attracted considerable attention. A variety of multi-axis force sensors have been developed for robotic applications, such as wrist rehabilitation, surgical needle insertion, minimally invasive surgery, robotic grasping and interaction. In these applications, the system overall cost is one of the major factors that hinder the wide application of them. Multi-axis force sensor is one of the high-cost items in above applications. Therefore, how to develop cost-effective force sensor has attracted considerable attention in recent years. The research work has covered developing new sensing principle as well as methods [13,19–21], design necessary degrees of freedom to meet the functional requirements and reduce the material costs [22]. In Refs. [13,19], a miniature Linear Series

* Corresponding author at: School of Aeronautics and Mechanical Engineering, Changzhou Institute of Technology, Changzhou, Jiangsu 213032, PR China.
E-mail addresses: huahl123@126.com, huahl@czu.cn (H. Hua).

Elastic Actuator (LSEA) has been developed to achieve grasping force perception and control. Since the LSEA utilizes the cost-effective linear spring and potentiometer to achieve force sensing, its overall cost could be significantly reduced when compared with the multi-axis force sensor. To address the inherent nonlinearity problem of the potentiometer, a rational Bezier Calibration Method (BCM) [21] and Sparse Piecewise Calibration Method (SPCM) [20] was developed to further enhance the force perception accuracy of the LSEA. By adjusting the configuration of the spring, the LSEA could be easily transferred into a rotary type [23,24] to expand its applicability. The merit of this approach is that the force measurement unit could be highly integrated with the actuator. The drawback is that its generality is still limited. In Ref. [22], a novel highly sensitive shear force measurement method has been proposed that uses the eccentricity of two cylinders, and an ultra-miniature six-axis force sensor has been developed to achieve grasping force perception. Thanks to the simple manufacturing process of the sensor structure, the force sensor could achieve low cost.

Since in some cases, only three dimensions force is needed, a six-axis force/torque sensor could result in a waste of resources [25]. Designing necessary degrees of freedom of the force sensor could reduce the cost to a certain extent. In Ref. [26], a one-axis miniature force sensor, which based on the complaint mechanism, has been developed to achieve medical puncture force perception. Since the stiffness of the complaint mechanism is relatively lower, the force measurement range is quite limited. The measurement range of the developed one-axis force sensor prototype is only about 6 N. In addition, its fabrication requires precision machining and assembly, which could still lead to a higher cost. Reviewing previous studies, it could be observed that the high cost of the force sensor is mainly attributed to the complex fabrication process, including material cutting requirement, strain gauge adhesion, and structural assembly. Recently, Mayetin [27,28] present a unique solution for reducing the cost of the multi-axis force sensor by utilizing the standardized and modular force gauge unit, which could provide a new approach for developing cost-effective force sensors.

Besides the hardware cost, the force-based control strategy is also an important aspect in the interactive applications. Reviewing literatures, we found that previous studies about the human-robot interaction mainly focus on the robot impedance control, the literature concerning how to achieve compliant object transfer between human and robot is still few. Impedance control was firstly proposed in [29,30]. In impedance control, the robot is viewed as an impedance element, such as a spring-damper-mass system, which is connected to a complex external environment [31]. The principle of robot impedance control is to control the force and motion of robots when they come into contact with the environment by sensing the force and position of the robot's end effector. Once the robot detects the change in contact force or motion with the environment, the impedance controller will calculate the force that the robot needs to apply based on the impedance model parameters, and adjusts the robot's position and speed accordingly to achieve good interaction effects. At present, the application of impedance control in compliant object transfer is quite difficult. On the one hand, the impedance control is a highly model-based control approach, and its control performance is quite sensitive to the environmental factors [31,32]. During the dynamic control process, the model parameters can change accordingly, which could lead to the control instability [33]. During the object transfer process, the load of the robot will change suddenly, which could further increase the potentials of control stability and lead to the problem of safety. On the other hand, in some applications with a high real-time requirement, such as robotic object transfer and polishing,

complex model solving process of the impedance controller could lead to a long delay in force generation and affect the interaction quality [34]. Therefore, achieving compliant human-robot object transfer through impedance control is still challenging.

There are two main differences between the compliant human-robot object transfer control and robot impedance control. On the one hand, the control object of the impedance control is robot. While in object transfer control, the control object is a robotic gripper, which is installed on a multi-axis force sensor. On the other hand, to guarantee the safety of the interaction, the object transfer operation is generally performed at the stationary status of the robot. In Refs. [16,35], a vision-learning-based interactive control strategy has been developed for transferring object between human and robot. In these studies, the object is characterized as light (generally the gravity is less than 2 N) and small sized. The object is transferred from the robot to the human hand by simply open the grasping mechanism and release the object. In transferring mass object, this manner could lead to the security risk. Since the large object gravity will be applied to the human hand in an instant during the object releasing process, while the human hand requires a certain of time to respond to the transient load of the object. As a result, the object will be more easily to be slipped from the human hand. Up to now, from the best knowledge of authors, there is no literature reporting for the force-based compliant object transfer control strategy, especially for the mass object transfer.

1.2. Research motivation

The primary motivation of this research work is to develop a compliant, and cost-effective interactive grasping system for the object transfer operation between human and robot. The interactive force between the object and the human hand is measured by a novel modular 3-axis force sensor, which is characterized as easy to fabricate and cost-effective. Compliant object transfer control strategy has been proposed based on the measured interactive force to achieve compliant object transfer. The novelty of the proposed interactive grasping system includes,

(1) A modular 3-axis force sensor, which is composed of three modular force gauges, is presented. The modular force gauge is standardized and cost-effective, which could structure a 3-axis force sensor with a simple fabrication process. Only simple planar machining, laser cutting and assembly are required. The total cost of the 3-axis force sensor is less than 8\$. A comparison of the force (or torque) sensors between the previous studies and our design is summarized in Table A1, which is a continuous enrichment of Ref. [28]. It could be observed from Table A1, that only two of them, including ours and Ref. [28], have been developed in a modular manner, which has the advantages of flexible and easy to restructure to adapt to different measurement situations. Compared to Ref. [28], the proposed force sensor has a novel configuration. The force gauges in our design are connected in an end-to-end and orthogonal manner. This configuration is characterized as low coupling between each axis. The signal of each axis could be easily decoupled utilizing the classical decoupling theory as introduced in Ref. [36]. Therefore, the proposed force sensor has three advantages over the others in Table A1, those are: (1) ultra cost-effective, (2) easy to decoupling, and (3) modular structure.

(2) A compliant object transfer control strategy, which is composed of incremental force control mode and gravity balance control mode, is proposed for the human-robot interactive operations. Previous studies mainly focused on the light and small sized object transfer between human and robot [16,35]. In addition, those interactive control strategies are vision-based approach. Mass object compliant transfer between the human and robot has

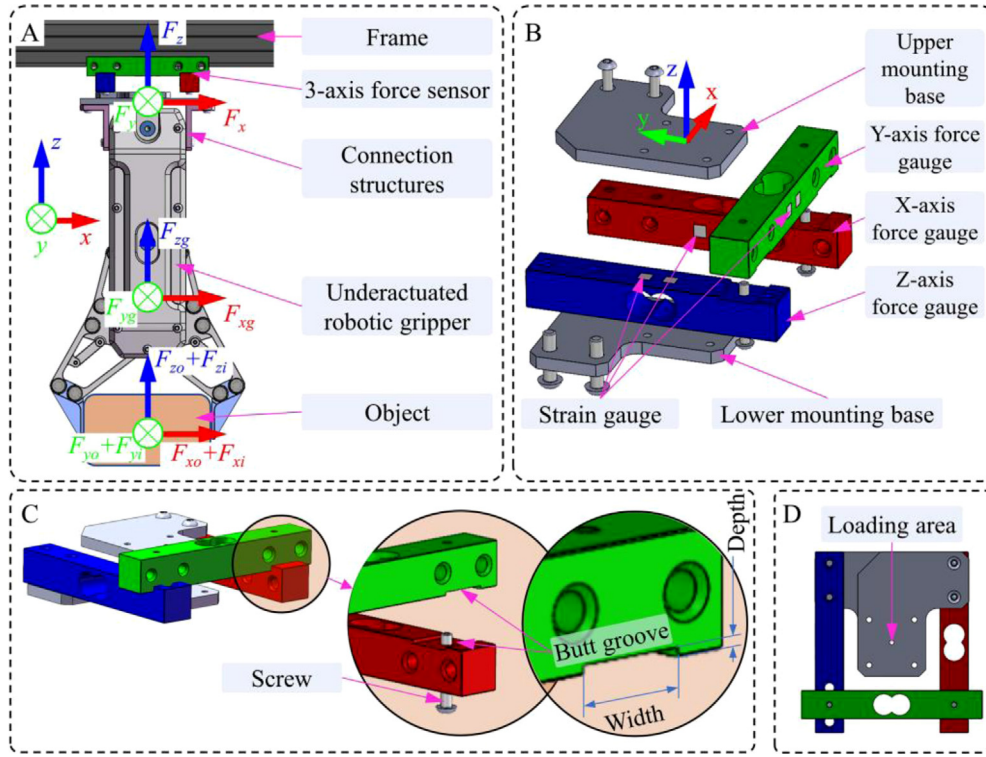


Fig. 1. Illustration of the interactive grasping system based on the modular 3-axis force sensor (A). (B) Construction of the modular 3-axis force sensor. (C) Assembly details of the modular force gauge. (D) Top view of the modular 3-axis force sensor.

not been addressed in previous studies. Faced with this problem, the proposed control strategy utilizes multi-interactive control mode, those are incremental force control mode and gravity balance control mode, to address the mass object transfer problem. In this way, objects with different weight could be transferred from the robotic gripper to the human hand in a more compliant manner.

The rest of this paper is organized as following. Section 2 presents the hardware description of the proposed interactive grasping system. Calibration method of the 3-axis force sensor is described in Section 3. Compliant object transfer control strategy is introduced in Section 4, which is then experimentally validated in Section 5. Experimental results are discussed in Section 6. Section 7 presents the conclusions.

2. Hardware description

2.1. Structural design

As displayed in Fig. 1A, the grasping system is mainly composed of an underactuated robotic gripper and modular 3-axis force sensor. The underactuated robotic gripper is installed on the lower side of the 3-axis force sensor through connection structures. The upper side of the 3-axis force sensor is fixed on the frame. The construction of the proposed modular 3-axis force sensor is displayed in Fig. 1B, which is mainly composed of three independent force gauges and two mounting bases. The nominal rated load capacity of the force gauge is 10 Kg.

The three force gauges are connected in a perpendicular manner and form a U-shaped structure as depicted in Fig. 1D. To enhance the bearing capacity of the U-shaped structure, a butt groove is designed on the assembly surface of the force gauge. For this assembly method, the butt groove should be well designed. A larger butt groove width could lead to the connection to be easily shifting, while smaller butt groove width could lead to

the interference and difficult to assemble. Furthermore, a precise process requirement could increase the fabrication cost. A feasible approach is to design the tolerance zone of the butt groove width as 0 to +0.1 mm and increase its depth. In this way, the fabrication cost could be reduced. In fabrication, we have observed that a larger depth is beneficial to eliminate the assembly clearance and enhance the rigidity of the connection. In the present study, the butt groove depth is designed as 2 mm. Two L-shaped mounting bases are connected to the two ends of the U-shaped force gauge and form a compact square structure. In the present design, the loading area of the mounting bases is designed at the geometric center of the 3-axis force sensor to reduce the additional torque caused by the external load, as shown in Fig. 1D. Finally, the length, width and height of the 3-axis force sensor are 80 mm, 80 mm and 27.3 mm, respectively. The total cost of the proposed 3-axis force sensor is less than 8\$ including strain gauges, HX711 modules, MCU, manufactured mechanical components and electric components. The details of the above cost items are illustrated in Table 1.

During the grasping process, operation force $\mathbf{F}_g = [F_{xg} \ F_{yg} \ F_{zg}]^T$ of the gripper, object gravity $\mathbf{F}_o = [F_{xo} \ F_{yo} \ F_{zo}]^T$ and interaction force $\mathbf{F}_i = [F_{xi} \ F_{yi} \ F_{zi}]^T$, which is applied to the object by external environment, will be transmitted to the 3-axis force sensor and achieve an equilibrium with the reaction force of the 3-axis force sensor $\mathbf{F} = [F_x \ F_y \ F_z]^T$ as

$$\mathbf{F} = \mathbf{F}_g + \mathbf{F}_o + \mathbf{F}_i \quad (1)$$

where operation force \mathbf{F}_g includes the static and dynamic factors of the gripper.

2.2. Finite element analysis of the 3-axis force sensor

Finite element analysis has been performed to reveal the strain characteristic of the proposed 3-axis force sensor. Since the strain

Table 1
Cost items of the proposed 3-axis force sensor.

Cost items	Manufacturing	Pieces	Total price (\$)
Strain gauge	Direct buy	3	2.10
HX711 module	Direct buy	3	1.22
Upper/lower mounting base	Laser cutting	5	1.16
Screw	Direct buy	6	0.17
MCU (Arduino UNO)	Direct buy	1	2.33
Other electric components	Direct buy	–	0.73
Total costs			7.7\$

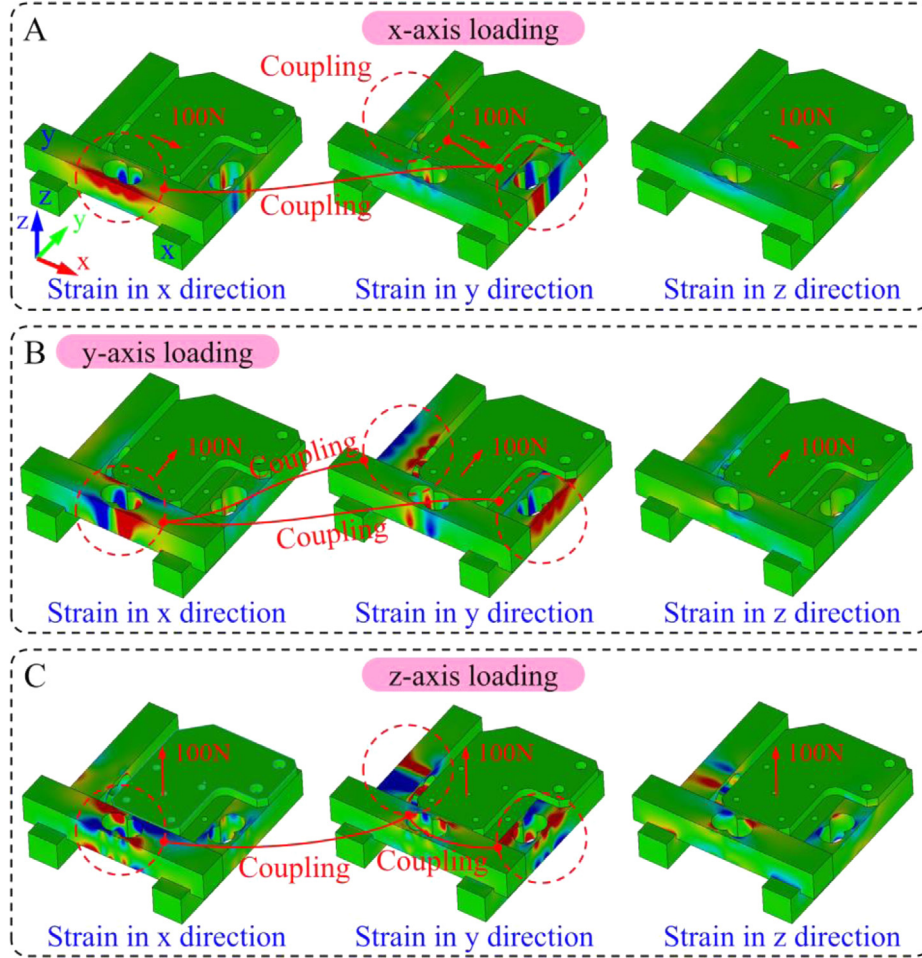


Fig. 2. FEM-based strain analysis of the 3-axis force sensor. (A) x-axis loading. The x-axis signal is dominated by the strain in y direction. (B) y-axis loading. The y-axis signal is dominated by the strain in x direction. (C) z-axis loading. The z-axis signal is dominated by the strain in y direction.

relation between each axial force is essential for determining the configuration of the proposed 3-axis force sensor, especially the relative installation direction between the triaxial force gauges. The material of the force gauges is aluminum alloy 7075, which has a tensile yield strength and Young's modulus of 503 MPa and 71.7 GPa, respectively. In simulation, the upper mounting base is fixed. An axial force of 100 N is applied to the lower mounting base in the x, y, and z-axis individually. Fig. 2 displays the strain distribution characteristic of the 3-axis force sensor under different loading conditions.

Since the strain gauges are attached to the surface of the force gauge, as depicted in Fig. 1B. They are more sensitivity to the tensile strain of the adhesive surface of the strain gauges. Therefore, both the x, y and z-axis strain component under different loading conditions has been computed and given in Fig. 2. For the present design, the x, y, and z-axis force are dominated by, x, and y directional strain, respectively. Results reveal that in the single-axis loading process, the strain is dominated by the

loading axis, in which the tensile and compression strain appear simultaneously. While in the other coupling regions, the strain is unidirectional in the adhesive direction of the strain gauges, it will produce a small signal when sampled by a full-bridge circuit. Therefore, the strain coupling between the x, y and z-axis is relatively weak. This characteristic is due to the orthogonal connection design between each two force gauges. The weak coupling characteristic between the x, y and z-axis is quite useful in actual measurement, since it is easy to be addressed using the classical decoupling model as introduced in Ref. [36].

3. Calibration of the 3-axis force sensor

In developing the proposed 3-axis force sensor, we have observed that the cost-effective force gauge product has not been well calibrated. The individual difference of the force gauges could lead to the measurement error of the triaxial forces. Under

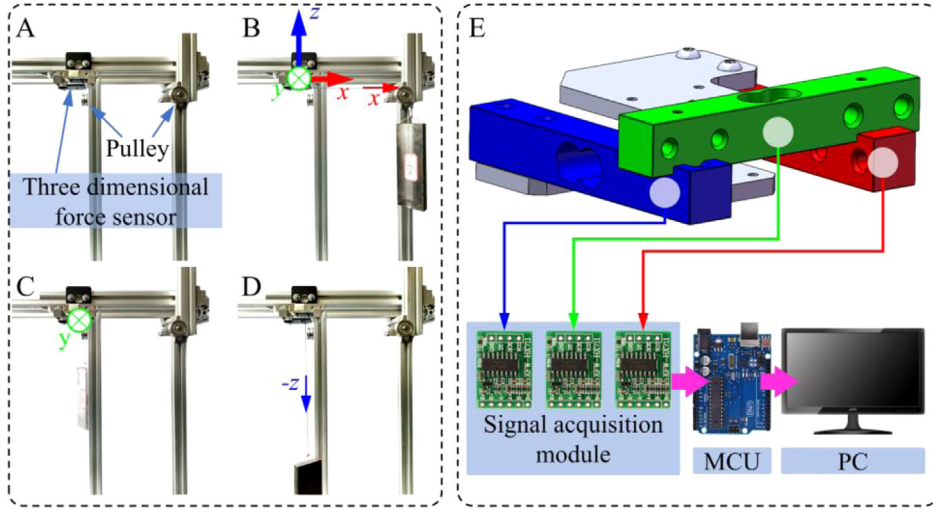


Fig. 3. Experimental calibration of the 3-axis force sensor. (A) Experimental platform. (B) x-axis loading. (C) y-axis loading. (D) -z-axis loading. (E) Signal acquisition system.

this circumstance, the theoretical relationship of triaxial forces could not provide an effective support for developing the decoupling model of the 3-axis force sensor. Therefore, the most feasible way is to identify the decoupling matrix of the three-axis force sensor and experimentally evaluate its measurement performance to provide a guide for the measurement applications.

3.1. Single-axis calibration

According to the calibration theory, the actual force of the 3-axis force sensor \mathbf{F} could be computed by the axial force vector \mathbf{f} as [36]

$$\mathbf{F} = \mathbf{C}\mathbf{f} \quad (2)$$

where $\mathbf{f} = [f_x \ f_y \ f_z]^T$, and f_x, f_y, f_z denote the calibrated force of the x, y, and z-axis force gauge. \mathbf{C} denotes the decoupling matrix. The calibration of f_x, f_y and f_z could be given as

$$f_x = \frac{f_{x0} - x_{off}}{x_{amp}}, \quad f_y = \frac{f_{y0} - y_{off}}{y_{amp}}, \quad f_z = \frac{f_{z0} - z_{off}}{z_{amp}} \quad (3,4,5)$$

where f_{x0}, f_{y0} and f_{z0} denote the original value of the x, y, and z-axis force gauge signal, respectively. $x_{amp}, y_{amp}, z_{amp}$ and $x_{off}, y_{off}, z_{off}$ denote the gain and offset coefficients of f_{x0}, f_{y0} and f_{z0} , respectively.

(1) Offset coefficients identification

Take into consideration the fluctuation characteristics of the measured f_{x0}, f_{y0} and f_{z0} , the offset coefficients are identified by computing the average value of the data stream as

$$x_{off} = \frac{\sum_{i=1}^n f_{x0,i}}{n}, \quad y_{off} = \frac{\sum_{i=1}^n f_{y0,i}}{n}, \quad z_{off} = \frac{\sum_{i=1}^n f_{z0,i}}{n} \quad (6,7,8)$$

where i denotes the time series, n denotes the length of the data stream. Since x_{off}, y_{off} and z_{off} could be affected by the specific application scenario, Eqs. (6)–(8) are compiled into a specific functional routine, which could be executed independently to fulfill the requirements under different application scenario. In this way, the sensor calibration and the subsequent application will be more convenient. Because some undesired disturbance, such as the effect of sensor tilt status, signal drifting and hysteresis, could be removed in one go without the requirement of additional compensation modeling.

(2) Gain coefficients identification

The gain coefficients, those are x_{amp}, y_{amp} and z_{amp} , respectively, could be computed by

$$x_{amp} = \frac{\Delta f_{x0}}{\Delta F_x}, \quad y_{amp} = \frac{\Delta f_{y0}}{\Delta F_y}, \quad z_{amp} = \frac{\Delta f_{z0}}{\Delta F_z} \quad (9,10,11)$$

where, $\Delta F_x, \Delta F_y$ and ΔF_z denote the incremental force which applied to the 3-axis force sensor in the x, y and z-axis directions, respectively. $\Delta f_{x0}, \Delta f_{y0}$ and Δf_{z0} denote the corresponding response variation of the force gauge.

To obtain the gain coefficients of the force gauge, an experimental platform is established as displayed in Fig. 3A. The upper side of the 3-axis force sensor is fixed on the frame. Two pulleys, which are mounted on the same horizontal height as the lower mounting base of the 3-axis force sensor are utilized to apply the load in the x and y-axis direction as depicted in Fig. 3B and Fig. 3C, respectively. The z-axis load is applied by hanging the weight block directly as depicted in Fig. 3D. The signal acquisition system is displayed in Fig. 3E. Three HX711 modules, which are cost-effective 24 bit Analog-to-Digital Converter (ADC), are utilized to sample the electrical signal from the x, y, and z-axis force gauges independently.

In the present study, $\Delta F_x, \Delta F_y$ and ΔF_z are set as 7.71 N, 7.71 N and -7.71 N, respectively, by a steel block with a gravity of 7.71 N as depicted in Fig. 3B–Fig. 3D. The gravity of the steel block is measured by an electronic balance, which has a measurement accuracy of 1×10^{-4} N. The corresponding loading response of the 3-axis force sensor is displayed in Fig. 4. From the response it could be observed that $\Delta f_{x0}, \Delta f_{y0}$ and Δf_{z0} are about 182307.50 N, 182142.81 N and -186728.03 N, respectively. According to Eqs. (9)–(11), $x_{amp}, y_{amp}, z_{amp}$ are computed as 23645.59, 23624.23 and 24218.94, respectively. It should be noted that x_{amp}, y_{amp} , and z_{amp} are dimensionless gain coefficients, which could map the original value of the x, y, and z-axis force gauge signal to the true value directly.

3.2. Decoupling matrix identification

The decoupling matrix \mathbf{C} could be identified by performing the single-axis loading test by three times and collect the obtained F_x, F_y, F_z and f_x, f_y, f_z as

$$\underbrace{\begin{bmatrix} F_{x1} & F_{x2} & F_{x3} \\ F_{y1} & F_{y2} & F_{y3} \\ F_{z1} & F_{z2} & F_{z3} \end{bmatrix}}_{\mathbf{F}_e} = \underbrace{\begin{bmatrix} c_{11} & c_{12} & c_{13} \\ c_{21} & c_{22} & c_{23} \\ c_{31} & c_{32} & c_{33} \end{bmatrix}}_{\mathbf{C}} \underbrace{\begin{bmatrix} f_{x1} & f_{x2} & f_{x3} \\ f_{y1} & f_{y2} & f_{y3} \\ f_{z1} & f_{z2} & f_{z3} \end{bmatrix}}_{\mathbf{f}_e} \quad (12)$$

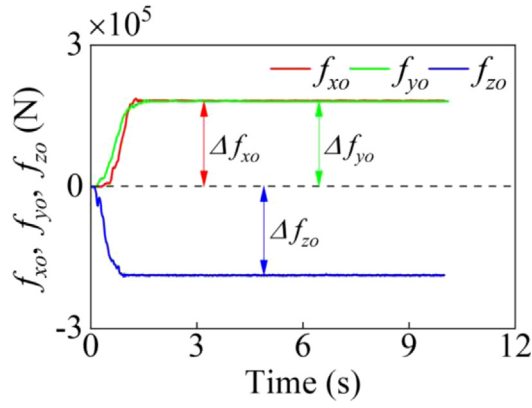


Fig. 4. Steady-state response of the x, y, and z-axis force gauges under a certain load before amplitude calibration.

where, the subscript 1, 2 and 3 denote the test number. According to Eq. (12), the decoupling matrix C could be identified as

$$C = F_e f_e^{-1} \quad (13)$$

Single-axis loading experiments are performed based on the experimental platform as depicting in Fig. 3. Steady-state response of the X, y and z-axis force gauge after gain and offset calibrations is measured by Eqs. (3)–(5), respectively, and displayed in Fig. 5.

According to Fig. 5, F_e and f_e could be obtained as

$$F_e = \begin{bmatrix} 7.71 & 0 & 0 \\ 0 & 7.71 & 0 \\ 0 & 0 & -7.71 \end{bmatrix}, \quad f_e = \begin{bmatrix} 7.71 & 0.31 & -0.02 \\ -0.15 & 7.71 & -0.05 \\ 0.00 & 0.24 & -7.71 \end{bmatrix} \quad (14,15)$$

respectively. According to Eqs. (13) to (15), the corresponding decoupling matrix C could be identified as

$$C = \begin{bmatrix} 1.00 & -0.04 & 0.00 \\ 0.02 & 1.00 & 0.00 \\ 0.00 & 0.03 & 1.00 \end{bmatrix} \quad (16)$$

3.3. Model validation and measurement performance test

(1) Validation of the calibration model

Single-axis and multi-axis loading experiments have been performed to verify the effectiveness of the calibration model, that is Eq. (2), based on the identified decoupling matrix C . In single-axis loading experiments, a steel block with a gravity of 7.71 N is utilized to apply load to the force sensor in different directions independently. The obtained response of the coupled and decoupled responses is compared in Fig. 6.

Fig. 6A, Fig. 6B and Fig. 6C are x, y, and z-axis responses, respectively. In which, the red, green, and blue transparent area denote the x, y and z-axis loading process, respectively. Comparing Fig. 6A–Fig. 6C, it could be observed that in the y-axis loading process, the x and z-axis measurement, those are f_x and f_z , are disturbed by the y-axis load by about 0.294 N and 0.239 N, respectively. This means that the y-axis is significantly coupled with the x and z-axis. After calibration, the coupling error of F_x , F_y and F_z could be greatly reduced. The residual coupling error is about 0.01 N and 0.03 N.

In multi-axis loading experiments, two steel blocks with different gravity are utilized to evaluate the effectiveness of the calibration models. The gravity of two steel blocks is 7.71 N and 12.8 N, respectively. The corresponding loading response as well as the calibration results is given in Fig. 7. Results reveal that in multi-axis loading process, the calibration model is still effective. The residual calibration error of the x, y and z-axis is about 0.005 N, 0.004 N, and 0.0145 N, respectively. Therefore, the calibration model and the identified decoupling matrix, those are Eqs. (2) and (16) are valid.

(2) Measurement performance test

Linearity, hysteresis, and repeatability of the proposed 3-axis force sensor are tested based on the experimental platform as

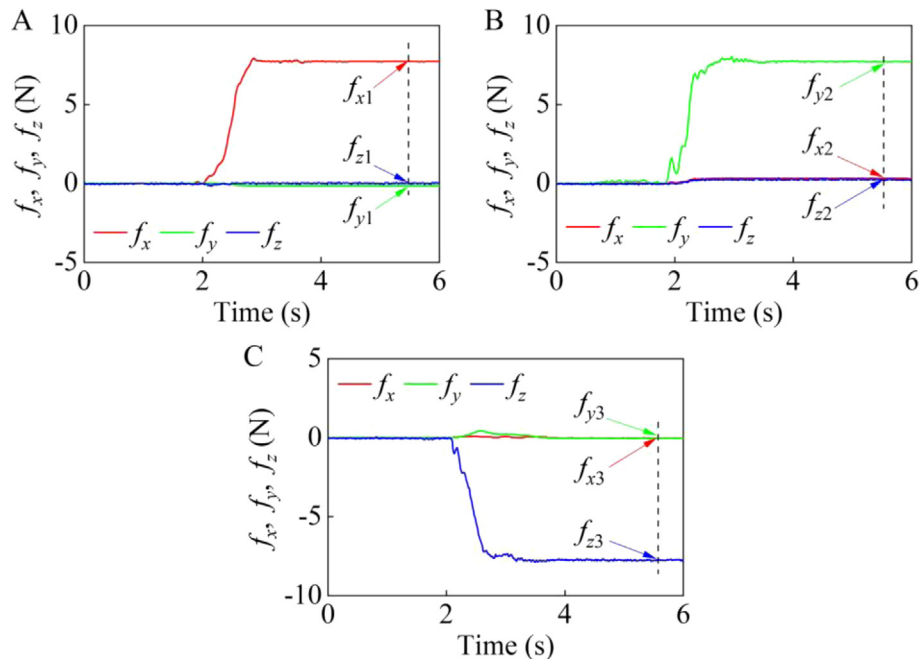


Fig. 5. Steady-state response of the x, y, and z-axis force gauges under single-axis loading. (A) x-axis response. (B) y-axis response. (C) z-axis response.

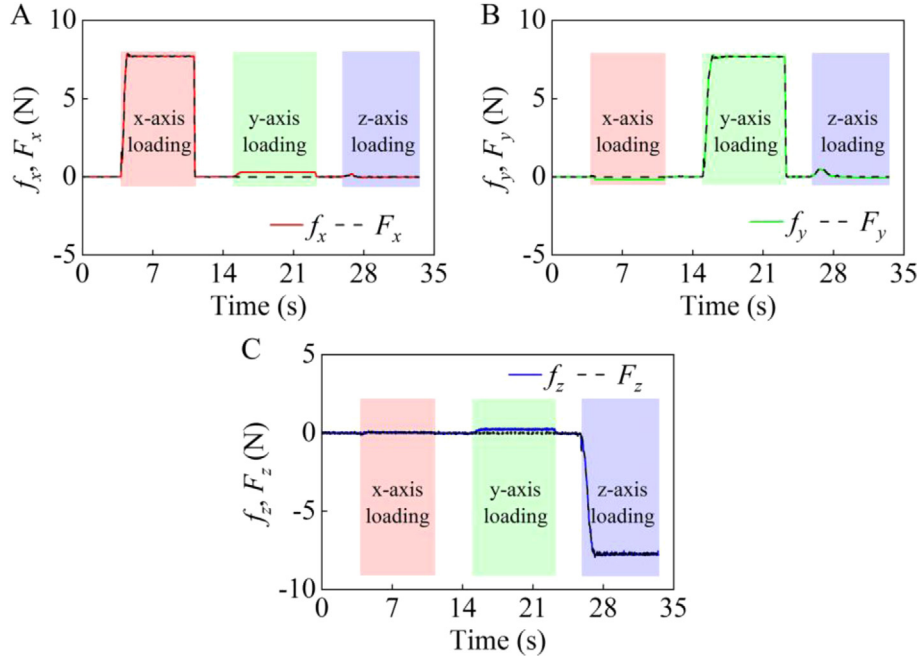


Fig. 6. Steady-state response of the single-axis loading validation experiments. (A–C) Comparisons of the original and decoupled response of the x, y, and z-axis, respectively. (For interpretation of the references to color in this figure legend, the reader is referred to the web version of this article.)

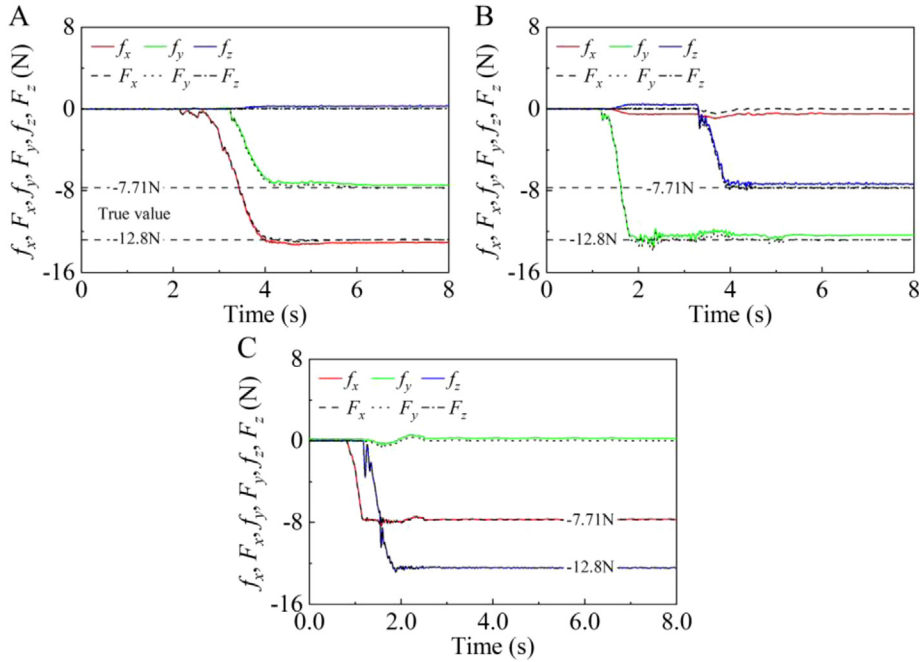


Fig. 7. Steady-state response of the multi-axis loading validation experiments. (A) x and y axis loading. (B) y and z axis loading. (C) x and z axis loading.

depicted in Fig. 3A. Since the force gauges are standardized products, their nominal measurement range is about 98 N. To avoid damaging the force sensor, the linearity, hysteresis, and repeatability tests are performed within the range of 0–80 N by adjusting the number of the steel blocks, which has an average gravity of 7.71 N. The experimental results of linearity, hysteresis, and repeatability errors of x, y, and z-axis are summarized in Table 2. It reveals that the maximum linearity, hysteresis, and repeatability

errors is 3.93%, 2.77%, and 1.73%, respectively, which could basically fulfill the requirement of human-robot interaction [23]. In Ref. [28], a low-cost, modular force sensor has been developed utilizing the similar approach as this study. Its maximum linearity, hysteresis, and repeatability errors is 4.76%, 3.2%, and 2.4%, respectively. Compared to Ref. [28], our design has smaller error peak values under a larger measurement range. This could be attributed to the advantages of the orthogonal connection

Table 2

Experimental results of linearity, hysteresis, and repeatability errors of different loading axis.

Force	Linearity error (%)	Hysteresis error (%)	Repeatability error (%)
F_x	3.71	2.61	1.70
F_y	3.62	2.49	1.62
F_z	3.93	2.77	1.73

design between each two force gauges in this study, the mutual disturbance between the x, y, and z-axis could be greatly reduced and improve the overall measurement performance.

4. Compliant object transfer control strategy

To endow the robotic gripper with compliant object transfer ability, two kinds of interactive control mode, including incremental force control and gravity balance control, are developed based on the modular 3-axis force sensor, as depicted in Fig. 8. In object transfer control, the grasping and releasing motions of the underactuated gripper are controlled by the servo valve through a voltage instruction u_g . During the object transfer control, the incremental force control and gravity balance control modes are determined based on the infinite norm of the measured \mathbf{F} and a threshold value F_{mode} , which could be given by an external controller.

(1) Incremental force control mode

In incremental force control mode, Eqs. (6)–(8), (3)–(5) and (2) will be executed in sequence. Where Eqs. (6)–(8) denote the zeroing operation, which could remove the effect of the operation force \mathbf{F}_g and the gravity of the object \mathbf{F}_o on \mathbf{F} . Therefore, the output of Eq. (2) will depend directly on the external interactive force \mathbf{F}_i . Then, the releasing motion of the robotic gripper is controlled by

$$u = \begin{cases} u_g & \text{if } \|\mathbf{F}\|_\infty < f_{\text{threshold}} \\ 0 & \text{if } \|\mathbf{F}\|_\infty \geq f_{\text{threshold}} \end{cases} \quad (17)$$

where, $f_{\text{threshold}}$ denotes the control threshold of the voltage. If $\|\mathbf{F}\|_\infty < f_{\text{threshold}}$, the control voltage of the servo valve is set as u_g to maintain the grasping state of the object. During the interaction, \mathbf{F}_i will appear and lead to the increment of \mathbf{F} . As \mathbf{F} fulfill $\|\mathbf{F}\|_\infty \geq f_{\text{threshold}}$, u will be set as 0 to release the object and achieve interactive operation.

(2) Gravity balance control mode

As depicting in Fig. 8, in gravity balance control mode, Eq. (2) is utilized to measure the external force directly without zeroing operation. In this circumstance, the measured \mathbf{F} will depend on two components, those are object gravity \mathbf{F}_o and interactive force \mathbf{F}_i as

$$\mathbf{F} = \mathbf{F}_o + \mathbf{F}_i \quad (18)$$

In gravity balance control, the releasing motion of the robotic gripper is controlled by

$$u = \begin{cases} u_g & \text{if } \|\mathbf{F}\|_\infty \geq f_{\text{threshold}} \\ 0 & \text{if } \|\mathbf{F}\|_\infty < f_{\text{threshold}} \end{cases} \quad (19)$$

During the interaction, $\|\mathbf{F}\|_\infty$ will decrease once an interactive force \mathbf{F}_i is applied to the object in the opposite direction of \mathbf{F}_o . Theoretically, $\|\mathbf{F}\|_\infty = 0$ could be fulfilled when the interactive force \mathbf{F}_i achieve an equilibrium with the object gravity \mathbf{F}_o . However, due to the fluctuation characteristic of the external interactive force, it is difficult to achieve $\|\mathbf{F}\|_\infty = 0$ in real time interaction. Therefore, a positive $f_{\text{threshold}}$ is utilized to switch the control state of the robotic gripper. In addition, $f_{\text{threshold}}$ should be smaller than that of the gravity of the object to guarantee the grasping stability.

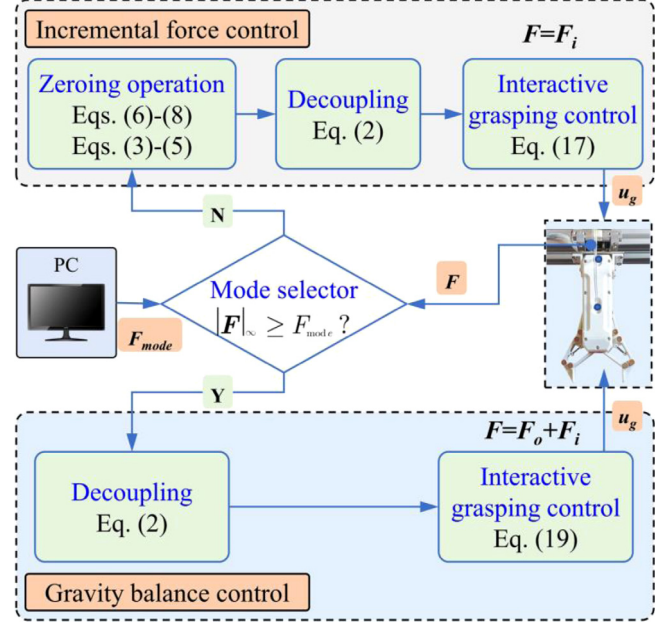


Fig. 8. Illustration of the control structure of the interactive grasping.

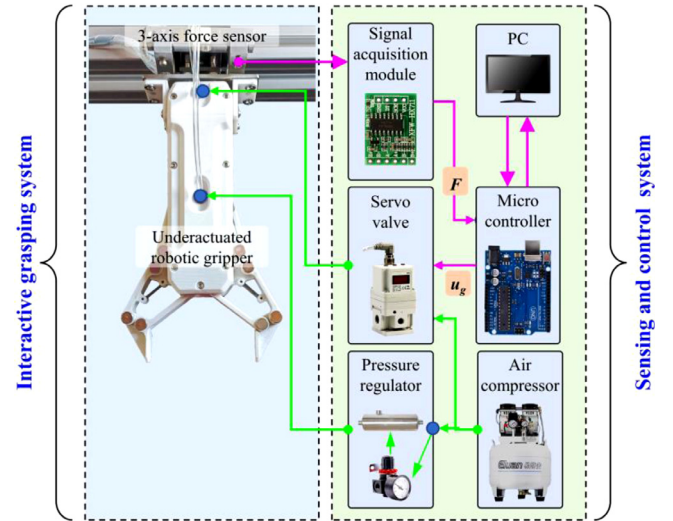


Fig. 9. Grasping control system.

5. Grasping control

5.1. Experimental setup

A grasping experimental platform, as depicting in Fig. 9, is established to perform grasping control experiments based on the proposed modular 3-axis force sensor. A pneumatic underactuated robotic gripper, which is actuated by a servo valve, is utilized to perform grasping operations. Pressure of the servo valve is controlled by an Arduino UNO micro controller using

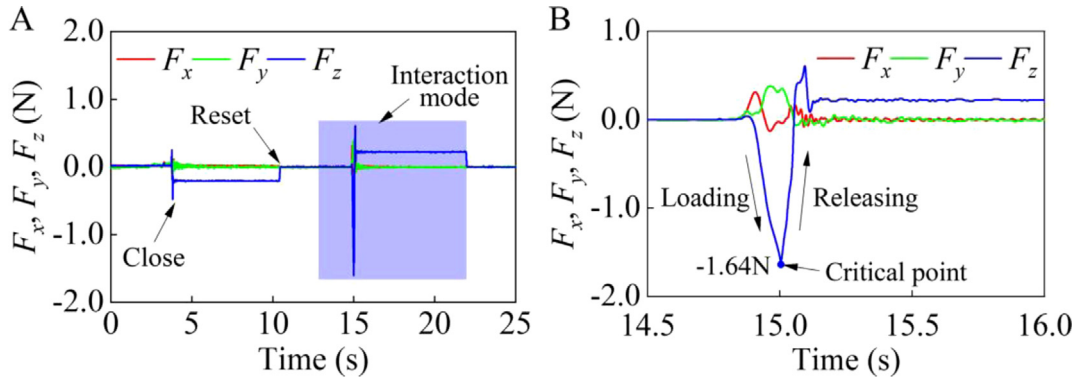


Fig. 10. Interactive force response of grasping a soft packing bag (A) and its enlarged view (B).

Pulse Width Modulation (PWM) signal. The releasing motion of the robotic gripper is actuated by a constant restoring pressure, which is adjustable by a regulator. To maintain the stability of the restoring pressure, a pressure buffer bottle with a volume of 350 mL is installed between the robotic gripper and pressure regulator. To guarantee the real-time control performance, the calibration models of the 3-axis force sensor are compiled into C code and executed on the micro controller. A PC is utilized to set the control instructions.

5.2. Incremental force control test

(1) Multidirectional interactive force control test

In this section, the effectiveness of the incremental force control strategy, that is Eq. (17), is investigated experimentally. In experiment, u_g is set as 3.0 V to actuate the robotic gripper to produce a grasping force of about 5 N to perform grasping operations. A typical interactive response of a soft packing bag, which has a gravity of about 0.2 N, is displayed in Fig. 10A. The corresponding grasping and interactive process is depicted in Fig. 11. It could be observed that after the closure of the finger mechanism, the gravity of the object will be applied to the 3-axis force sensor, and F_z produce a negative offset of about -0.2 N. The corresponding grasping state is displayed in Fig. 11A. Then in about 10.5 s, the incremental force control mode is activated by the mode selector. The amplitude of F_z reduces to zero immediately due to the execution of Eqs. (6)–(8). This means that the effect of the object gravity on \mathbf{F} has been successfully filtered, and the measured \mathbf{F} is a direct reflection of the external interactive force \mathbf{F}_i .

In experiment, $f_{\text{threshold}}$ is set as 1.5 N to perform interactive control. Then in about 15 s, an external interactive force is applied to the object by a human finger, as depicted in Fig. 11B, in the $-z$ -axis direction. The corresponding interactive force response is depicted in Fig. 10B with an enlarged view. It could be observed that the amplitude of F_z increases gradually and achieve a peak value of about 1.64 N during the interaction. According to Eq. (17), u will be switched from u_g to 0 when \mathbf{F} fulfills $\|\mathbf{F}\|_{\infty} \geq f_{\text{threshold}}$, and the robotic gripper will open its finger mechanism to release the object. After the releasement of the object, the amplitude of F_z will reduce immediately and produce a positive offset of about 0.2 N, which is equal to the object gravity. Finally, in about 22 s, a zeroing instruction is given to the micro controller to reset the measurement of \mathbf{F} for next grasping and interaction control.

As described in Eq. (17), in incremental force control mode, the grasping control is depended on the infinite norm of \mathbf{F} . Each component of \mathbf{F} or their combination could be utilized to control the grasping motion. In following a similar interactive grasping control experiment is performed to evaluate the multi-dimensional interactive ability of the grasping system. In experiment, the object is a stack of napkin, which also has a gravity of about

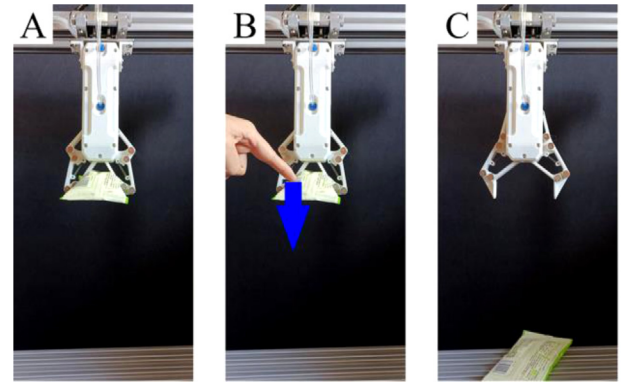


Fig. 11. Grasping and interaction process of a soft packing bag. (A) Steady-state of the grasping. (B) Interaction with a human finger. (C) Object releasing.

0.2 N. The corresponding interaction force response and grasping process are displayed in Fig. 12 and Fig. 13, respectively. In interactive control process, the human finger holds the object and apply an interactive force to the object in the x -axis direction as shown in Fig. 13B. As F_x exceeds 1.5 N, the gripper will open to release the object.

It should be noted, that the settling time of \mathbf{F} depends on the loading speed of human hand rather than that of the limitation of the measurement system. To exhibit the interactive control process clearly, the interactive force is applied in a slower manner in this study. After the releasement of the object, some components of \mathbf{F} , especially F_z , could appear a sharp point, as depicted in Fig. 10B and Fig. 12B, respectively. This phenomenon is due to a sudden stop of the finger mechanism as it moves to its travel limit. As a result, the shock will transfer to the wrist force sensor and be captured by the z -axis force gauge of the force sensor.

(2) Human-robot interaction test under tilt status

To further verify the effectiveness of the incremental force control mode under tilt status, the interactive grasping system is installed on a manipulator to perform multi status switching and object transfer operations with human hand. At first, a circular object with a gravity of 0.9 N is fed into the grasping range of the finger mechanism and grasped by the gripper, as shown in Fig. 14A, in which the status of the gripper is vertical. As a result, F_z produces a negative offset of about -0.9 N, as shown in Fig. 14F. Then in Fig. 14B and Fig. 14C, the robotic gripper moves with the manipulator to rotate from the vertical status to the horizontal one in sequence. In this process, the measurement of F_x and F_z will be disturbed. This is because the overall gravity direction of the robot gripper is constant. As the status of the gripper and wrist force sensor varies, the loading direction of the

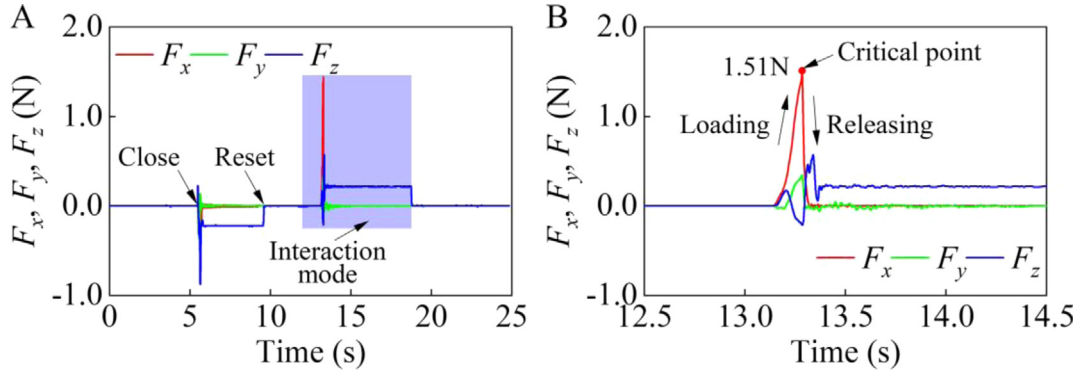


Fig. 12. Grasping response of a stack of napkins (A) and its enlarged view (B).

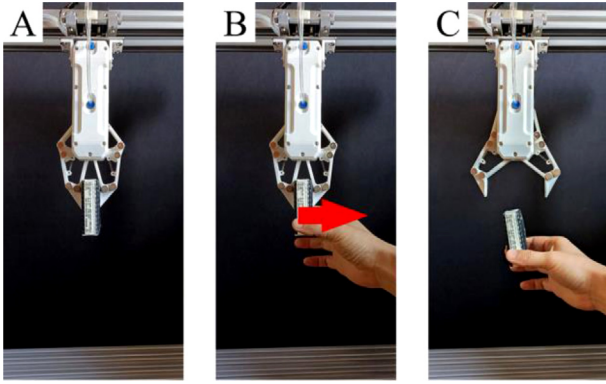


Fig. 13. Grasping and interactive process of a stack of napkin. (A) Steady-state of the grasping. (B) Interaction with a human finger. (C) Object releasing.

gripper gravity will vary accordingly. In Fig. 14(A–C), the zeroing operation is performed at 3.3 s, 6.7 s, and 9.4 s, respectively. Results reveal that the zeroing operation is effective.

In Fig. 14D, the robotic gripper moves back to the 45° tilt status to perform object transfer operation. In 11.5 s, the incremental force control mode is activated with a $f_{\text{threshold}}$ of 3 N. Then the human hand starts drag the object at 13.7 s in a natural manner and increase the interactive force gradually. In 13.9 s, \mathbf{F} fulfills $\|\mathbf{F}\|_{\infty} \geq f_{\text{threshold}}$ and the object is released by the gripper and be transferred to the human hand successfully, as depicted in Fig. 14E.

(3) Interactive sensitivity test

To evaluate the limit sensitivity of the interactive grasping system, a series of interactive force control experiments are performed under different $f_{\text{threshold}}$, which has a range of 0 N to 2 N. A typical grasping response is depicted in Fig. 15A. In interactive grasping force control, the human finger squeezes a corner of the soft packing and drag slightly in the $-z$ -axis direction as depicted in Fig. 16B. As F_z decrease to -0.22 N, the release control starts and the object is released from the robotic gripper. It could be observed from Fig. 15B that although the human finger applies load in the $-z$ -axis direction, F_x and F_y has achieved an equivalent peak amplitude, which are about 0.18 N and 0.16 N, respectively, as the amplitude of F_z increases. This means that F_x and F_y has the potentials to trigger the releasing control by mistake under the sensitivity of 0.2 N. Under this sensitivity, we found it is difficult for the human hand to quantitatively distinguish and control the loading direction of the interactive force. The main reason for this phenomenon is that both the finger-pulp and the object are soft, which will deform and produce a disturbance in the other directions during the interaction. Therefore, the grasping system has a limit sensitivity of about 0.2 N.

5.3. Gravity balance control test

In gravity balance control, a dumbbell with a gravity of 9.8 N is adopted as the grasping object. F_{mode} is set as 5 N to determine the interactive control mode, and $f_{\text{threshold}}$ is set as 0.1 N. The control response and interaction process are displayed in Fig. 17 and Fig. 18, respectively. During the experiment, the dumbbell is grasped by the robotic gripper and achieve a steady-state as depicted in Fig. 17A. Under the action of the object gravity, F_z produces an offset of about -9.8 N as displayed in Fig. 17A. As illustrated in Fig. 8, once $\|\mathbf{F}\|_{\infty} \geq F_{\text{mode}}$, the gravity balance control mode will be activated automatically. In 11.5 s, an interactive force in the z -axis direction is applied to the dumbbell gradually by a human hand as depicted in Fig. 18B. As the interactive force increases, the amplitude of F_z decrease gradually as depicted in Fig. 17B. In 13 s, the amplitude of F_z reduces to about 0.02 N and the robotic gripper releases the dumbbell as shown in Fig. 18C.

According to Eqs. (18) and (19), the interaction force \mathbf{F}_i will have an equivalent amplitude as the object gravity \mathbf{F}_o under the constraint $\|\mathbf{F}\|_{\infty} < f_{\text{threshold}}$. The actual difference between them depends on $f_{\text{threshold}}$. This means that during the object transfer process, the human hand could achieve a quasi-static equilibrium with the object as long as $f_{\text{threshold}}$ is small enough. In this way, the object could be transferred from the robotic gripper to the human hand without obvious impact.

6. Discussion

At present, the commercial multi-axis force sensor is relatively expensive, which is a one of the key factors that hinder the wide application of the robotic technology. For example, the cost of the six-axis force sensor FT300, which is adaptable to the famous Robotiq gripper, is about 5970\$. This kind of cost level is unaffordable for the majority of small (or medium)-sized enterprises, and medical rehabilitation patients. The total cost of the proposed 3-axis force sensor in the present study is less than 8\$, meanwhile the force measurement performance could basically fulfill the requirement of human–robot interaction. This is due to the novel design and configuration of the proposed 3-axis force sensor, which could also provide a novel view of designing multi-axis force sensor. Compare to the existing commercial multi-axis force sensor, the proposed 3-axis force sensor has decisive advantages and novelty.

The measurement speed of the 3-axis force sensor is one of the key factors in the interactive applications. In the present study, the cost-effective HX711 ADC modules, which has a limit sampling frequency of 80 Hz, are utilized to sample the response of the force gauges. The single sampling time of the ADC module is about 12.5 ms. Therefore, in computing the offset coefficients, those are Eqs. (9)–(11), the length of the data stream n should

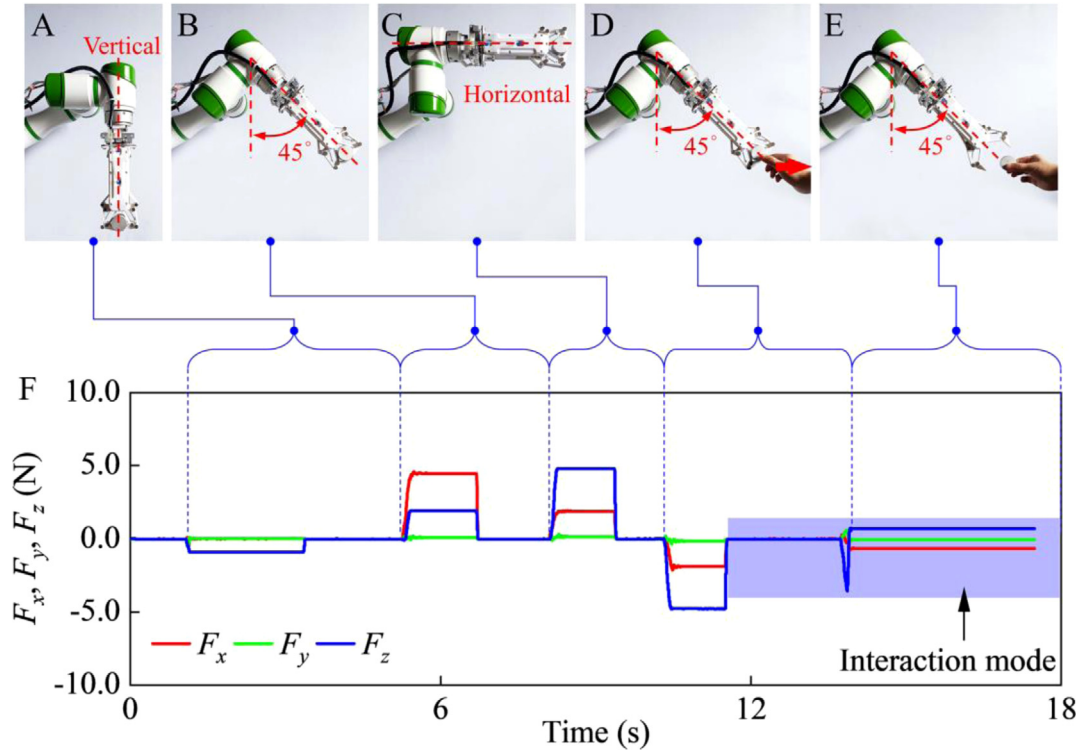


Fig. 14. Human-robot interaction under tilt status. (A–C) Multi status switching and disturbance filtering. (D) and (E) Robot to human object transfer. (F) Response of the interactive force.

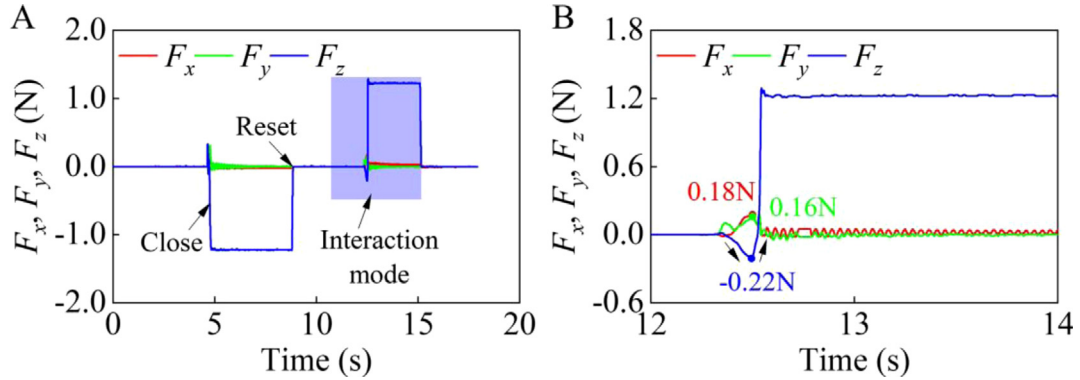


Fig. 15. Grasping response of a soft packing (A) and its enlarged view (B).

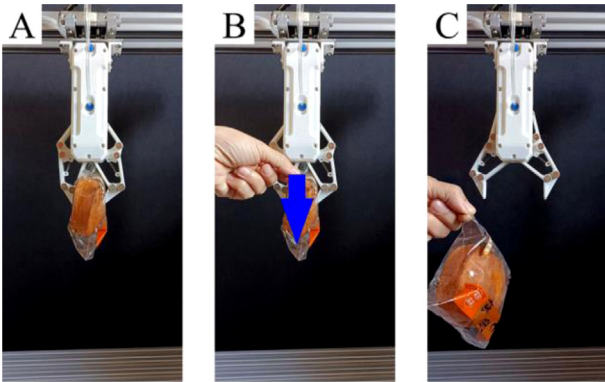


Fig. 16. Grasping and interactive process of a soft packing. (A) Steady-state of the grasping. (B) Interaction with a human finger. (C) Object releasing.

be carefully determined to fulfill real time measurement requirements. In the present experiments, n is set as 5 to balance the effectiveness of zeroing operation and real time measurement requirement. Interactive grasping experiments have revealed that the measurement model of the 3-axis force sensor could basically fulfill the real time interactive control.

Generally, lower model computational complexity is benefit for reducing the algorithm data occupation and the overall computing cost. This could enable the control strategy to be executed on a more cost-effective micro controller with limited computational ability. Object transfer control rules, those are Eqs. (17) and (19), are based on the computing of $\|\mathbf{F}\|_\infty$, its computational complexity is relatively lower. According to the actual test, it has been observed that the computing cost of $\|\mathbf{F}\|_\infty$ on Arduino UNO is about 0.01 ms, its effect on real-time control is negligible. It is worth noting that the Arduino UNO is an 8-bit micro controller, and its price is only 2.33\$. Finally, human-robot interactive control experiments, which are presented in Section 5,

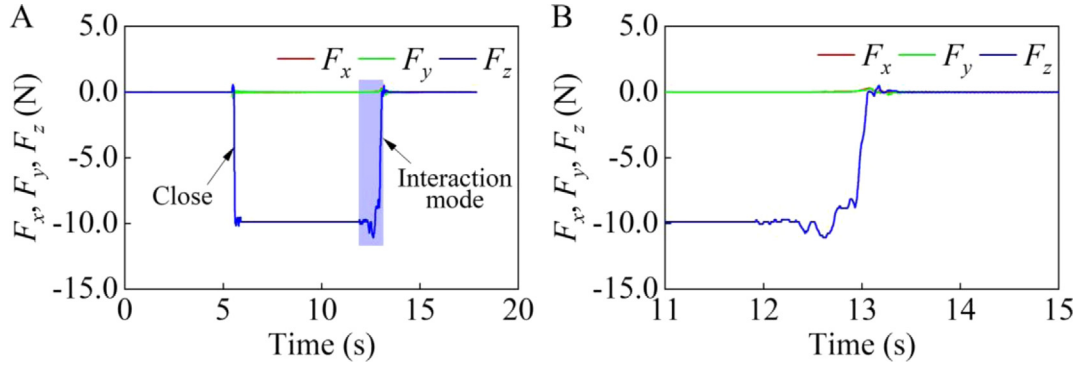


Fig. 17. Grasping and interactive response of a dumbbell with a gravity of 9.8 N using gravity balance control mode (A) and its enlarged view (B).

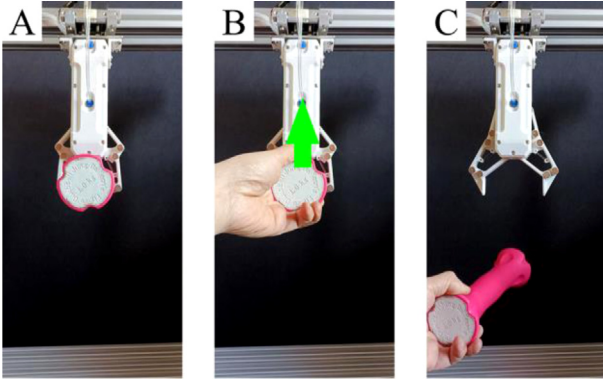


Fig. 18. Transfer process of a dumbbell. (A) Steady-state of the grasping. (B) Interaction with a human hand. (C) Object releasing.

have demonstrated that the control strategy could be successfully executed on Arduino UNO and achieve compliant object transfer.

Two control modes are presented for the interactive grasping control, those are incremental force control and gravity balance control. Since the object gravity will be applied to the human hand in an instant during the releasing process, the human hand requires a certain time to respond to the transient load of the object. Therefore, the incremental force control mode is more suitable for the lighter objects. A larger $f_{\text{threshold}}$ is benefit for the human hand to distinguish the actual loading direction during the interactive control and achieve accurate operation. However, increase $f_{\text{threshold}}$ could increase the interactive force applied to the object, which could aggravate the balance between the object and the human hand during the object transfer process. Reducing $f_{\text{threshold}}$ could increase the sensitivity of the interactive force control and deliver object in a more compliant manner. Experimental results reveal that the fabricated interactive object transfer system has a limit sensitivity of about 0.2 N. As $f_{\text{threshold}}$ decrease to 0.2 N, it will be difficult for the human hand to quantitatively distinguish the actual loading direction of the interactive force. Therefore, the interactive control index, that is $\|F\|_{\infty}$, could be replaced by its components, such as $|F_x|$, $|F_y|$, $|F_z|$ or their combination to filter the disturbance from the undesired axis and enhance the interactive control performance.

For the heavier objects, the gravity balance control mode is more appropriate. In gravity balance control mode, the human hand could achieve a quasi-static equilibrium with the object during the object transfer process. Therefore, the object could be transferred to the human hand in a more compliant manner. The critical point between the lighter and heavier objects is about 0.5 Kg, which is determined by performing a variety of interactive experiments. It could also be modified by adjusting F_{mode} to adapt to the actual object transfer situation.

7. Conclusions

This paper presents the interactive object transfer control of an undereducated robotic gripper based on a modular 3-axis force sensor. Calibration method of the modular 3-axis force sensor is described in detail and validated experimentally. Compliant object transfer control strategy, which is composed of incremental force control mode and gravity balance control mode, is proposed for the human-robot interactive operations.

Experimental results reveal that the calibration model of the modular 3-axis force sensor is valid. The computation of the offset coefficients is a time-consuming operation due to the limitation of the sampling frequency of the HX711 module. To fulfill the real time measurement requirements in the interactive grasping, the length of the data stream n is set as 5 to balance the efficiency of zeroing operation and real time measurement performance, which is experimentally demonstrated to be reasonable. In addition, the HX711 module could also be replaced by some ADC chips with higher sampling frequency, such as AD7794, to enhance the measurement performance of the multi-axis force sensor in future work.

In the present study, the fabricated object transfer system has a limit interactive sensitivity of about 0.2 N. The incremental force control mode and gravity balance control mode are suitable for the interaction of light and heavy objects, respectively. In gravity balance control mode, the human hand could achieve a quasi-static equilibrium with the object during the transferring process. In this way, the heavy object could be transferred to the human hand in a more compliant manner without obvious impact.

Declaration of competing interest

The authors declare that they have no known competing financial interests or personal relationships that could have appeared to influence the work reported in this paper.

Acknowledgments

This research is funded by the China Postdoctoral Science Foundation under Grant 2022M721613, National Natural Science Foundation of China under Grant 62273061.

Appendix. A tabular review of the state-of-the-art multi-axis force sensor

See Table A.1.

Table A.1
Comparison of force sensors [28].

Studies about F/T sensors	Measurement capability	Design purpose	Measurement approach	Force limits	Dimensions (mm)	Producing and assembly complexity	Producing cost	Modularity	Electronics
ATI Nano25 [37]	3 axis force 3 axis torque	General robotics	Piezoresistive	Fx, Fy \pm 250 N Fz \pm 1000 N	$\Phi 25 \times 21.6$	Precision machining precision assembly	Very high	–	Separated
Kim, 2001 [38]	3 axis force 3 axis torque	General	Piezoresistive	Fx, Fy, Fz 100 N	–	Precision machining precision assembly	Higher	–	Separated
Song et al. 2007 [39]	3 axis force 1 axis torque	Wrist rehabilitation	Piezoresistive	Fx, Fy, Fz \pm 20 N	$> \Phi 60 \times 12$	Precision machining precision assembly	Higher	–	Separated
Kim, 2007 [40]	3 axis force 3 axis torque	Intelligent robot wrist	Piezoresistive	Fx, Fy, Fz \pm 200 N	$\Phi 100 \times 31$	Precision machining precision assembly	Higher	–	Separated
Jacq et al. 2010 [41]	3 axis force 3 axis torque	Wrist rehabilitation	Piezoresistive	Fx, Fy 1000 N Fz 200 N	$\Phi 68 \times 7$	Simple planar machining precision assembly	Lower	–	Separated
Kim et al. 2010 [42]	3 axis force 3 axis torque	Finger muscular strength	Piezoresistive	Fx, Fy, Fz 100 N	$82 \times 82 \times 18$	Precision machining precision assembly	Higher	–	Separated
Kim et al. 2012 [43]	3 axis force 3 axis torque	Finger force measurement	Piezoresistive	Fx, Fy, Fz 200 N	$\Phi 67 \times 32$	Precision machining precision assembly	Higher	–	Separated
Wu et al. 2013 [44]	3 axis force 3 axis torque	General	Piezoresistive	Fx, Fy, Fz 20 N	$\Phi 52 \times 28$	Precision machining precision assembly	Higher	–	Separated
Ma et al. 2013 [45]	3 axis force 3 axis torque	General	Piezoresistive	Fx, Fy \pm 100 N Fz 100 N	–	Precision machining precision assembly	Higher	–	Separated
Wang et al. 2013 [46]	3 axis force 3 axis torque	Robotic wrist applications	Piezoresistive	Fx, Fy 100 N Fz 200 N	$> \Phi 100 \times 70$	Precision machining precision assembly	Higher	–	Separated
Jacq et al. 2014 [47]	3 axis force 3 axis torque	Wrist rehabilitation	Piezoresistive	Fx, Fy, Fz 250 N	–	Simple machining simple assembly	Lower	–	Separated
Yuan et al. 2015 [48]	3 axis force 3 axis torque	Humanoid robot foot	Piezoresistive	Fx, Fy 400 N Fz 1000 N	$\Phi 50 \times 12$	Precision machining	Higher	–	Separated
Liang et al. 2016 [49]	3 axis force 3 axis torque	Cutting force measurement	Piezoresistive	Fx, Fy \pm 350 N Fz \pm 500 N	$\Phi 80 \times 42$	Precision machining	Higher	–	Separated
Guggenheim et al. 2016 [50]	3 axis force 3 axis torque	General	MEMS Barometer	Fx \pm 4 N, Fy \pm 5 N Fz 10 N	$75 \times 75 \times 16$	Simple machining simple assembly	Higher	–	Separated
Kim et al. 2017 [51]	3 axis force 3 axis torque	Robot applications	Capacitive	Fx, Fy, Fz \pm 50 N	$\Phi 25 \times 19$	Precision machining	Higher	–	Integrated
Grosu et al. 2017 [52]	3 axis force	Pelvis interaction forces for rehabilitation	Piezoresistive	Fx, Fy 60 N Fz 2000 N	$80 \times 80 \times 96$	Simple machining precision assembly	Higher	–	Separated
Xiong et al. 2018 [53]	3 axis force	Robot applications	Fiber Bragg	Fx, Fy \pm 50 N Fz 60 N	$\Phi 72 \times 26$	Precision machining precision assembly	Higher	–	Separated
Kebede et al. 2019 [54]	3 axis force 3 axis torque	General robotics	Piezoresistive	Fx, Fy, Fz 100 N	–	Precision machining precision assembly	Higher	–	Separated
Umut Mayetin and Serdar Kucuk, 2021 [28]	3 axis force	Wrist rehabilitation	Piezoresistive	Fx, \pm 100 N, Fy \pm 40 N Fz \pm 20 N	$\Phi 62 \times 70$	Simple machining simple assembly	Lower	Modular	Integrated
Our design	3 axis force	Human–robot object transfer	Piezoresistive	Fx, Fy, Fz \pm 80 N	$80 \times 80 \times 28$	Simple machining simple assembly	Lower	Modular	Separated

References

- [1] Realysvázquez-Vargas A, Arredondo-Soto KC, García-Alcaraz JL, Márquez-Lobato BY, Cruz-García J. Introduction and configuration of a collaborative robot in an assembly task as a means to decrease occupational risks and increase efficiency in a manufacturing company. *Robot Comput-Integr Manuf* 2019;57:315–28.
- [2] Cherubini A, Passama R, Crosnier A, Lasnier A, Fraisse P. Collaborative manufacturing with physical human–robot interaction. *Robot Comput-Integr Manuf* 2016;40:1–13.
- [3] Li J, Guan Y, Chen H, Wang B, Zhang T, Liu X, Hong J, Wang D, Zhang H. A high-bandwidth end-effector with active force control for robotic polishing. *IEEE Access* 2020;8:169122–169135.
- [4] Hong J, Wang D, Guan Y. Synergistic integrated design of an electrochemical mechanical polishing end-effector for robotic polishing applications. *Robot Comput-Integr Manuf* 2019;55:65–75.
- [5] Chen F, Zhao H, Li D, Chen L, Tan C, Ding H. Contact force control and vibration suppression in robotic polishing with a smart end effector. *Robot Comput-Integr Manuf* 2019;57:391–403.
- [6] Mohammad AEK, Hong J, Wang D. Design of a force-controlled end-effector with low-inertia effect for robotic polishing using macro-mini robot approach. *Robot Comput-Integr Manuf* 2018;49:54–65.
- [7] Zhong B, Cao J, McDaid A, Xie SQ, Zhang M. Synchronous position and compliance regulation on a bi-joint gait exoskeleton driven by pneumatic muscles. *IEEE Trans Autom Sci Eng* 2020;17:2162–6.
- [8] Freitas B, Silva M, Carvalho Ó, Renjewski D, Fonseca J, Flores P, Espregueira-Mendes J. Design, modelling and control of an active weight-bearing knee exoskeleton with a series elastic actuator. In: 2019 IEEE 6th Portuguese Meeting on Bioengineering. ENBENG, IEEE; 2019. p. 1–4.
- [9] Chen T, Casas R, Lum PS. An elbow exoskeleton for upper limb rehabilitation with series elastic actuator and cable-driven differential. *IEEE Trans Robot* 2019;35:1464–74.
- [10] Li Z, Huang B, Ye Z, Deng M, Yang C. Physical human–robot interaction of a robotic exoskeleton by admittance control. *IEEE Trans Ind Electron* 2018;65:9614–24.
- [11] Huy NP, Curtis S, Nuthi SG, Vale NM, Panagiotis P. Soft poly-limbs: Toward a new paradigm of mobile manipulation for daily living tasks. *Soft Robotics* 2019;6:38–53.
- [12] Valori M, Scibilia A, Fassi I, Saenz J, Behrens R, Herbster S, Bidard C, Lucet E, Magisson A, Schaake L, Robot Collaboration. Validating safety in human–Standards and new perspectives. *Robotics* 2021;10:65.
- [13] Hua H, Liao Z, Zhao J. Design, analysis, and experiment of an underactuated robotic gripper actuated by linear series elastic actuator. *J. Mechanisms and Robotics* 2022;15:021002.
- [14] Zhang Y, Huang Y, Ge Y, Bao N. A master–slave hand operation cooperative perception system for grasping object via information fusion of flexible strain sensors. *Measurement* 2021;169:108437.
- [15] Wang Y, Ding W, Mei D. Development of flexible tactile sensor for the envelop of curved robotic hand finger in grasping force sensing. *Measurement* 2021;180:109524.
- [16] Wang Y, Ewert D, Vossen R, Jeschke S. A visual servoing system for interactive human–robot object transfer. *J. Automation Control Engineering* 2015;3:283.
- [17] Liu Y, Li Z, Liu H, Kan ZJR, Systems A. Skill transfer learning for autonomous robots and human–robot cooperation: A survey. *Robot Auton Syst* 2020;128:103515.
- [18] Liu Y, Zhang Y, Yao Y, Zhong M. Laser point detection based on improved target matching method for application in home environment human–robot interaction. In: 2018 11th International Workshop on Human Friendly Robotics. HFR, IEEE; 2018. p. 13–8.
- [19] Hua H, Liao Z, Wu X, Chen Y, Feng C. A back-drivable linear force actuator for adaptive grasping. *J Mech Sci Technol* 2022;36:4213–20.
- [20] Hua H, Liao Z, Song J, Liu Y. A sparse piecewise calibration method for potentiometer with inherent nonlinearity: A comparison study. *Measurement* 2022;204:112033.
- [21] Hua H, Liao Z, Wu X, Chen Y. A bezier based state calibrating method for low-cost potentiometer with inherent nonlinearity. *Measurement* 2021;178:109325.
- [22] Kim U, Jeong H, Do H, Park J, Park C. Six-axis force/torque fingertip sensor for an anthropomorphic robot hand. *IEEE Robot Autom Lett* 2020;5:5566–72.
- [23] Hua H, Song J, Liao Z, Zhao J. Design and experiment of miniature linear series elastic actuator for robotic grasping. *Trans Chin Soc Agric Mach* 2022;53:500–6.
- [24] Hua H, Liao Z, Chen Y, Xu C. Design and test of compact series elastic force actuator for grasping mechanism. *Trans Chin Soc Agric Mach* 2021;52:426–32, 442.
- [25] Guo Y, Kong J, Liu H, Xiong H, Li G, Qin L. A three-axis force fingertip sensor based on fiber bragg grating. *Sensors Actuators A* 2016;249:141–8.
- [26] Shi C, Tang Z, Wang S. Design and experimental validation of a fiber bragg grating-enabled force sensor with an ortho-planar spring-based flexure for surgical needle insertion. *IEEE Transactions on Medical Robotics and Bionics* 2021;3:362–71.
- [27] Mayetin U, Kucuk S. Design and experimental evaluation of a low cost, portable, 3-DOF wrist rehabilitation robot with high physical human–robot interaction. *J Intell Robot Syst* 2022;106:1–22.
- [28] Mayetin U, Kucuk S. A low cost 3-DOF force sensing unit design for wrist rehabilitation robots. *Mechatronics* 2021;78:102623.

- [29] Hogan N. Adaptive control of mechanical impedance by coactivation of antagonist muscles. *IEEE Transactions on Automatic Control* 1984;29:681–90.
- [30] Hogan N. Impedance control an approach to manipulation. I- Theory. II- implementation. III -applications, transaction of the ASME. *Journal OfDynamic Systems, Measurement, and Control* 1985;107:1–24.
- [31] Duan J, Gan Y, Chen M, Dai XJR, Systems A. Adaptive variable impedance control for dynamic contact force tracking in uncertain environment. 102, 2018, p. 54–65.
- [32] Li X, Liu Y-H, Yu HJA. Iterative learning impedance control for rehabilitation robots driven by series elastic actuators. 90, 2018, p. 1–7.
- [33] Bogdanovic M, Khadiv M, Righetti L. Learning variable impedance control for contact sensitive tasks. *IEEE Robotics and Automation Letters* 2020;5:6129–36.
- [34] Fan C, Hong GS, Zhao J, Zhang L, Zhao J, Sun L. The integral sliding mode control of a pneumatic force servo for the polishing process. *Precis Eng* 2019;55:154–70.
- [35] Yang W, Paxton C, Cakmak M, Fox D. Human grasp classification for reactive human-to-robot handovers. In: 2020 IEEE/RSJ International Conference on Intelligent Robots and Systems. IROS, IEEE; 2020, p. 11123–30.
- [36] Templeman JO, Sheil BB, Sun T. Multi-axis force sensors: A state-of-the-art review. *Sensors Actuators A* 2020;304:111772.
- [37] ATI industrial automation, force /torque sensors, model Nano25, “https://www.ati-ia.com/products/ft/ft_models.aspx?id=Nano25”, Last Access (30.10.2020)..
- [38] Kim G-S. The design of a six-component force/moment sensor and evaluation of its uncertainty. *Meas Sci Technol* 2001;12:1445.
- [39] Song A, Wu J, Qin G, Huang W. A novel self-decoupled four degree-of-freedom wrist force/torque sensor. *Measurement* 2007;40:883–91.
- [40] Kim G-S. Design of a six-axis wrist force/moment sensor using FEM and its fabrication for an intelligent robot. *Sensors Actuators A* 2007;133:27–34.
- [41] Jacq C, Lüthi B, Maeder T, Lamercy O, Gassert R, Ryser P. Thick-film multi-DOF force/torque sensor for wrist rehabilitation. *Sensors Actuators A* 2010;162:361–6.
- [42] Kim G-S, Kim H-M, Kim H-I, Pio M-G, Shin H-S, Yoon J. Development of 6-axis force/moment sensor for measuring the fingers’ muscular strength of human. In: 2010 IEEE International Symposium on Industrial Electronics. IEEE; 2010, p. 428–33.
- [43] Kim H-M, Yoon J, Kim G-S. Development of a six-axis force/moment sensor for a spherical-type finger force measuring system. *IET Science, Measurement & Technology* 2012;6:96–104.
- [44] Wu B, Cai P. Decoupling analysis of a sliding structure six-axis force/torque sensor. *Measurement Science Review* 2013;13:187.
- [45] Ma J, Song A. Fast estimation of strains for cross-beams six-axis force/torque sensors by mechanical modeling. *Sensors* 2013;13: 6669–86.
- [46] Wang Z, Li Z, He J, Yao J, Zhao Y. Optimal design and experiment research of a fully pre-stressed six-axis force/torque sensor. *Measurement* 2013;46:2013–21.
- [47] Jacq C, Maeder T, Emery S, Simoncini M, Meurville E, Ryser P. Investigation of polymer thick-film piezoresistors for medical wrist rehabilitation and artificial knee load sensors. *Procedia Eng* 2014;87:1194–7.
- [48] Yuan C, Luo L-P, Yuan Q, Wu J, Yan R-J, Kim H, Shin K-S, Han C-S. Development and evaluation of a compact 6-axis force/moment sensor with a serial structure for the humanoid robot foot. *Measurement* 2015;70:110–22.
- [49] Liang Q, Zhang D, Coppola G, Mao J, Sun W, Wang Y, Ge Y. Design and analysis of a sensor system for cutting force measurement in machining processes. *Sensors* 2016;16:70.
- [50] Guggenheim JW, Jentoft LP, Tenzer Y, Howe RD. Robust and inexpensive six-axis force–torque sensors using MEMS barometers. *IEEE/ASME Trans Mechatronics* 2017;22:838–44.
- [51] Kim U, Lee D-H, Kim YB, Seok D-Y, Choi HR. A novel six-axis force/torque sensor for robotic applications. *IEEE/ASME Trans Mechatronics* 2016;22:1381–91.
- [52] Grosu V, Grosu S, Vanderborght B, Lefeber D, Rodriguez-Guerrero C. Multi-axis force sensor for human–robot interaction sensing in a rehabilitation robotic device. *Sensors* 2017;17:1294.
- [53] Xiong L, Jiang G, Guo Y, Liu H. A three-dimensional fiber bragg grating force sensor for robot. *IEEE Sens J* 2018;18:3632–9.
- [54] Kebede GA, Ahmad AR, Lee S-C, Lin C-Y. Decoupled six-axis force–moment sensor with a novel strain gauge arrangement and error reduction techniques. *Sensors* 2019;19:3012.